RSC Advances

PAPER

View Article Online
View Journal | View Issue

Cite this: *RSC Adv.*, 2017, **7**, 8167

Synthesis and characterization of a core–shell $BiVO_4$@g-C_3N_4 photo-catalyst with enhanced photocatalytic activity under visible light irradiation†

Zisheng Zhang,[ac] Miao Wang,[a] Wenquan Cui*[b] and Hong Sui*[ad]

Received 5th December 2016
Accepted 19th January 2017

DOI: 10.1039/c6ra27766g

www.rsc.org/advances

Novel core–shell structured ellipsoid-like $BiVO_4$@g-C_3N_4 composites, with different amounts of g-C_3N_4, have been successfully prepared by a simple hydrothermal-chemisorption method. Their performance as photocatalysts was systematically evaluated during RhB degradation under visible light irradiation. The composite with 7 wt% g-C_3N_4 was found to be 7 times more efficient as a photocatalyst than pristine $BiVO_4$. Its core–shell structure and activity were also found to be highly stable after it was used for 5 times in RhB degradation. The new composites were examined by various characterization techniques. The core–shell structure enhanced the contact area between the $BiVO_4$ core and g-C_3N_4 nano-sheet shell, which provided more active sites and strengthened the chemical band interaction. The thin g-C_3N_4 nano-sheets reduced the charge carrier transfer distance, which further suppressed the recombination of the photo-induced electron–hole pairs and therefore enhanced the photocatalytic activity of the composites. A reaction mechanism of the photocatalytic RhB degradation was proposed and discussed in detail.

1. Introduction

Photocatalytic technology has attracted the interest of many researchers since Fujishima and Honda[1] decomposed water into H_2 on a TiO_2 electrode in 1972. It[2–4] can serve as a solution to the global energy crisis and environmental pollution. Semiconductor photo-catalysts,[5] such as metal oxides, sulfides, and ternary materials with appropriate band gaps and high activity as well as stability, have attracted worldwide attention. However, some of them are only active when illuminated with ultra-violet (UV) light,[6,7] which only makes up 4% of solar-light, thus limiting their applications in reality. In addition, some photo-generated charge carriers go through recombination instead of leading to reactions, resulting in low photocatalytic activity.[8] At present, the critical research area in photo-catalysis is to develop a visible-light responsive, highly efficient, and chemically stable photo-catalyst.

Among the numerous semiconductor photo-catalysts examined so far, Bi-based compounds such as BiOX (X = Cl, Br, I),[9–13] $BiWO_6$,[14] and $BiVO_4$ have received the most attention. Bismuth vanadate ($BiVO_4$) was identified as one of the most promising photo-catalysts under visible light irradiation because of its nontoxicity, narrow bandgap energy (E_g = 2.40 eV), and chemical stability.[15] Pure $BiVO_4$ had different morphologies and crystal forms.[16,17] However, all of them are in fact relatively poor in absorbing visible lights. There have been many attempts by researchers to achieve better performance of pollution degradation with $BiVO_4$. $BiVO_4$ with double crystal phases was obtained for more reactive species during photo-degradation,[18] in addition to studies on different morphologies.[19] Several reports demonstrate that $Cu_2O/BiVO_4$ p–n junction photo-catalyst,[20] $Ag_3PO_4/BiVO_4$,[21] $BiVO_4$/rGO,[22] core–shell $BiVO_4$@Bi_2O_3 (ref. 23) and $BiVO_4$@MoS_2,[24] achieved better stability and higher photocatalytic degradation efficiency. However, according to previous studies, the increase of photo-catalysis activity was limited and the morphology of composites was rarely changed.

g-C_3N_4 (graphene-like carbon nitride) has become one of the most promising novel photocatalytic materials. It is a π-conjugate 2D layered material that is non-toxic, metal-free, has a desirable band gap position as well as excellent thermal and chemistry stability, and a simple product synthesis.[25,26] It was first studied to split water for hydrogen production by Wang

[a]*School of Chemical Engineering and Technology, Tianjin University, Tianjin, 300072, PR China. E-mail: suihong@tju.edu.cn; Tel: +86-022-27404701*

[b]*College of Chemical Engineering, Hebei Key Laboratory for Environment Photocatalytic and Electrocatalytic Materials, North China University of Science and Technology, Tangshan, 063009, PR China. E-mail: wkcui@163.com; Tel: +86-315-2592169*

[c]*Department of Chemical and Biological Engineering, University of Ottawa, Ottawa, Canada*

[d]*National Engineering Research Centre for Distillation Technology, 300072, Tianjin, PR China*

† Electronic supplementary information (ESI) available. See DOI: 10.1039/c6ra27766g

et al.[27] Unfortunately, pure g-C_3N_4 has a high recombination rate of photo-excited charges, resulting in limited photo-degradation efficiency. Many reports have combined g-C_3N_4 with other suitable semiconductors to produce novel composite photo-catalysts. TiO_2/g-C_3N_4,[28,29] CdS/g-C_3N_4,[30,31] AgX/g-C_3N_4 (X = Br, I),[32] g-C_3N_4/$AgVO_3$,[33] CeO_2/g-C_3N_4 (ref. 34) and g-C_3N_4/Bi-based composites[35–37] have been studied and all had higher photocatalytic efficiency both in pollution degradation and hydrogen production. g-C_3N_4 nano-sheets[38] had better performance when compared with g-C_3N_4 polymer. With the protection of g-C_3N_4 nano-sheets, novel core–shell Ag_3PO_4@g-C_3N_4,[39] CdS@g-C_3N_4 nanowire, ZnO/g-C_3N_4 (ref. 40) photo-catalyst showed enhanced photocatalytic activity.

Several reports have shown various combinations of $BiVO_4$ and g-C_3N_4 including $BiVO_4$/g-C_3N_4 Z-scheme photo-catalyst,[41] sulfur-doped g-C_3N_4/$BiVO_4$,[42] and g-C_3N_4/$BiVO_4$.[43–45] These compositions had impressive activity in water oxidation, pollution degradation, and CO_2 reduction. Many attempts have been made to produce composite photo-catalysts with improved degradation efficiency including Z-scheme photo-catalysts, heterojunctions, and core–shell structures.[46] As far as we know, there are no reports on the synthesis and application of core–shell $BiVO_4$@g-C_3N_4 for pollution degradation. Herein, we coated thin g-C_3N_4 nano-sheets onto ellipsoid $BiVO_4$ by simple stirring-chemisorption while varying the wt% of g-C_3N_4 to prepare different $BiVO_4$@g-C_3N_4 (x wt%). The photocatalytic activity is assessed by decomposing rhodamine B under visible light. The influence of g-C_3N_4 content is investigated and discussed. A possible photo-degradation mechanism is investigated based on the results of characterization and activity evaluation.

2. Experimental

All chemicals used in the experiments are analytical grade and were used without further purification.

2.1. Synthesis of g-C_3N_4 and g-C_3N_4 nano-sheets

g-C_3N_4 was synthesized through thermal condensation.[47] 5 g of melamine were put into an aluminum crucible with a cover on and subsequently heated in a muffle furnace at a rate of 5 °C min^{-1} until the temperature reached 550 °C where it was maintained for 4 hours. After cooling down to the room temperature, the light-yellow g-C_3N_4 products were ground and collected.

To prepare the g-C_3N_4 nano-sheets, 0.2 g g-C_3N_4 powder was ultra-sonicated in 1000 mL distilled water for 24 hours followed by centrifugation to remove the un-exfoliated g-C_3N_4, resulting in g-C_3N_4 nano-sheets dispersed solution. The concentration of the g-C_3N_4 nano-sheet suspension is about 0.07 g L^{-1}.

2.2. Synthesis of $BiVO_4$

$BiVO_4$ was synthesized through a hydrothermal method.[48] In this process, bismuth nitrate ($Bi(NO_3)_3 \cdot 5H_2O$) and ammonium vanadate (NH_4VO_3) were used as the bismuth and vanadate sources. 1.98 g $Bi(NO_3)_3 \cdot 5H_2O$ were dissolved in 40 mL ethylene glycol, forming a homogeneous milk-white solution under magnetic stirring. Then, 0.98 g of NH_4VO_3 were dissolved in 40 mL hot water, forming an orange-yellow transparent solution. The above NH_4VO_3 solution was added into the $Bi(NO_3)_3$ solution dropwise under vigorous stirring and incubated for 30 min. The resulting solution was then transferred to 100 mL Teflon-lined stainless steel autoclave and maintained at 100 °C for 12 h. After cooling the reactor down to room temperature, the yellow precipitates were collected and washed three times with distilled water and ethyl alcohol. Finally, the products were dried at 80 °C in electric oven for 6 h and a yellowish $BiVO_4$ powder was obtained.

2.3. Synthesis of $BiVO_4$@g-C_3N_4 core–shell composite photo-catalyst

$BiVO_4$@g-C_3N_4 core–shell composite photo-catalysts were synthesized by vigorous-stirring chemisorption (Fig. 1). 0.2 g $BiVO_4$ were added into measured amounts of g-C_3N_4 nano-sheets suspension (0.07 g L^{-1}) followed by ultra-sonication for 60 minutes and stirring for 24 h. Various weight ratios of g-C_3N_4 to $BiVO_4$@g-C_3N_4 (x wt%) (x = 1, 3, 5, 7, 10) were prepared by tuning the volume of g-C_3N_4 nano-sheets between 40 mL, 90 mL, 150 mL, 200 mL, and 300 mL, respectively.

2.4. Characterization

The crystal structures and phase data for the prepared $BiVO_4$@g-C_3N_4 composite samples were detected by X-ray diffraction (XRD) using a Rigaku D/MAX2500 PC diffractometer with Cu-Kα radiation and an operating voltage and current of 40 kV and 100 mA, respectively. The morphology of the core–shell $BiVO_4$@g-C_3N_4 samples was investigated by scanning electron microscope (SEM) (Hitachi, S-4800) and transmission electron microscopy (TEM) (JEOL Ltd., JEM-2010). Energy dispersive X-ray spectroscopy (EDX) displayed the distribution of the composed elements. UV-vis light (UV-vis) diffuse reflectance spectra were recorded on a UV-vis spectrometer (Puxi, UV1901) with $BaSO_4$ used as the reference, based on the data, the band-gap energy of the samples could be concluded. A similar trend occurs when calculating the band-gap energy (E_g) according to the follow formula:

$$(\alpha h\nu)^n = A(h\nu - E_g)$$

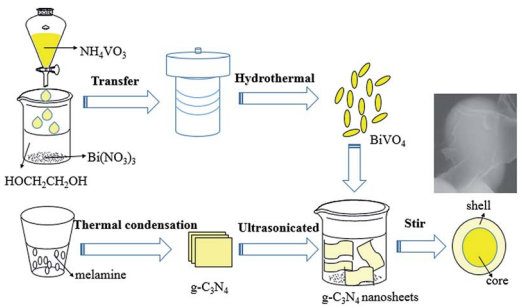

Fig. 1 The schematic illustration for $BiVO_4$@g-C_3N_4 synthesis process.

where α, h, ν, E_g and A respectively represent the absorption coefficient, Planck's constant, light frequency, band gap and a constant. The index, n, depends on the material and has a value of $n = 2$ for a direct-gap semiconductor and $n = 0.5$ for an indirect-gap semiconductor. The Fourier transform infrared spectra (FTIR) of the samples were recorded using an IR Vertex70 FTIR spectrometer from 4000–400 cm^{-1}. The chemical composition and the chemical states of the photo-catalysts were analyzed by X-ray photoelectron spectroscopy (XPS) using a XSAM 800 apparatus. Photoluminescence (PL) was performed on a fluorescence and phosphorescence lifetime and steady-state spectrometer (Edinburgh instruments FLSP 920, LED 360 nm). Electrochemical and photo-electrochemical measurements were performed in a constructed three electrode quartz cell system containing 0.5 M Na_2SO_4 electrolyte solution. Pt sheet was used as a counter electrode, Hg/Hg_2Cl_2/sat were used as reference electrodes, and a thin film of obtained samples on indium-tinoxide (ITO) was used as the working electrode for investigation. The photo-electrochemical experimental results were recorded with a CHI 660B electrochemical system.

2.5. Photocatalytic activity evaluation

The photocatalytic reaction of $BiVO_4$@g-C_3N_4 composite photo-catalyst under visible light was carried out by photodegradation of RhB. RhB is a very stable dye and has been used widely in evaluating the performance of numerous photo-catalysts under visible light irradiation. The photocatalytic reactions were carried out in quartz tubes (Nanjing, Xujiang), with a 3 cm distance from the light source. Visible light was supplied by a 400 W halogen lamp with cut-off filters for $\lambda \geq 420$ nm. 100 mg of the catalyst powder was dispersed into 50 mL of 10 mg L^{-1} RhB solution. The temperature of the reaction mixture was maintained at 25 ± 2 °C using a recirculating cooling water system. The suspension was stirred for 30 min in the dark to make ensure that the absorption–desorption equilibrium between the photo-catalyst and the RhB had been reached, at which point the light was turned on. 5 mL of the sample were taken out at constant time intervals during the reaction process over the course of 60 minutes. The samples were then centrifuged for 6 minutes at 10 000 rpm to remove the photo-catalyst powder. The supernatant was analyzed by UV-vis (TU-1901, Puxi) spectroscopy and the absorbance (A) was used to determine the concentration of RhB according to the Beer–Lambert law. The degradation efficiency of RhB was calculated by the following formula:

$$\text{Degradation } (\%) = \frac{C_0 - C}{C_0} \times 100\%$$

where C_0 represents the original concentration of RhB and C represents the concentration of RhB at time "t".

3. Result and discussion

3.1. XRD

XRD analysis was applied to evaluate the crystal phase of $BiVO_4$ and $BiVO_4$@g-C_3N_4 composites. Fig. 2 shows the XRD patterns

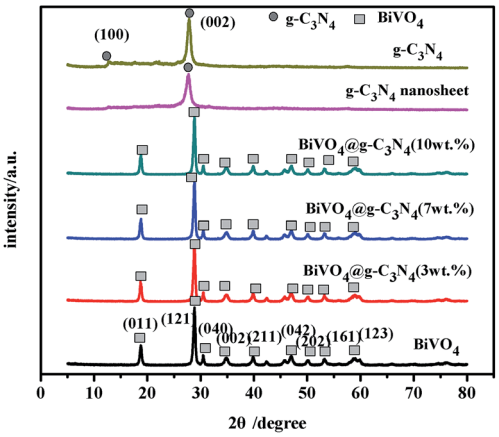

Fig. 2 XRD patterns of g-C_3N_4, $BiVO_4$ and $BiVO_4$@g-C_3N_4 with different g-C_3N_4 coated amounts.

of g-C_3N_4, $BiVO_4$, and $BiVO_4$@g-C_3N_4 with different coated amounts of g-C_3N_4 nano-sheets. For the pure g-C_3N_4, it can be clearly seen that the peaks at 12.8° and 27.8° correspond to the (100) and (002) diffraction planes (JCPDS 87-1526), respectively, which are characteristic of graphitic materials and fit well with reported literatures.[49] Where the (100) diffraction peak at 12.8° represents the in-plane structural packing motif of tri-*s*-triazine units, and the peak at 27.8° is indexed as (002) peak of the stacking of conjugated aromatic system, and the distance of interlayer spacing is 0.320 nm.[50] The XRD pattern of g-C_3N_4 nano-sheet obtained by ultra-sonicated shows only one obvious peak of (002), and the (002) diffraction peak of g-C_3N_4 nano-sheet is wider and weaker, indicating the stacking of inter-layer structure is broken and the exfoliated g-C_3N_4 nano-sheet is obtained.[39,51] As for $BiVO_4$, the observed peaks at 18.67°, 28.82°, 30.55°, 35.22°, 39.78°, 47.31°, 50.31°, 53.31° and 58.53° correspond to the (011), (121), (040), (002), (211), (042), (202), (161) and (123) crystal planes of m-$BiVO_4$ (JCPDS 14-0688).[17,48,52,53] The characteristic diffraction peaks were sharp, proving the better purity and crystallinity of $BiVO_4$. However, for the $BiVO_4$@g-C_3N_4 (x wt%) (x < 10) samples, only diffraction peaks of $BiVO_4$ were observed with no evidence of the existence of g-C_3N_4. This is likely due to small amounts of g-C_3N_4 nano-sheets being coated as well as the low diffraction intensity[22] of g-C_3N_4 in the composites. The existence of g-C_3N_4 can be shown through EDS, FT-IR and XPS, which is discussed later.

3.2. SEM & TEM analysis

The morphology and structure of the as-synthesized photo-catalysts were characterized by both scanning electron microscopy (SEM) and transmission electron microscopy (TEM). As shown in Fig. 3(a), bulk g-C_3N_4 had a layered structure, and the average size was about 2–3 μm, while the g-C_3N_4 nano-sheets treated by ultrasonication were much looser (Fig. 3(b)). The $BiVO_4$ precursor was a regular ellipsoid about 500 nm in diameter and 1–2 μm in length (Fig. 3(c)). For the $BiVO_4$@g-C_3N_4 (7 wt%) composites seen in Fig. 3(d) and (e), the thinner g-C_3N_4 nano-sheets can be seen coated on the ellipsoid-like

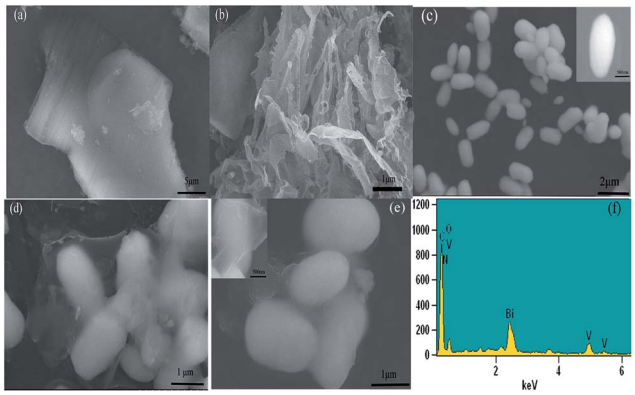

Fig. 3 SEM images of (a) g-C_3N_4; (b) g-C_3N_4 nano-sheets; (c) $BiVO_4$; (d) and (e) $BiVO_4$@g-C_3N_4; (f) the EDS for $BiVO_4$@g-C_3N_4 (7 wt%).

$BiVO_4$, the core–shell structure enlarges the contact area between the $BiVO_4$ and g-C_3N_4 nano-sheet, which benefits the transfer of photo-excited charge and enlarges the light absorption areas. More details about the core–shell structure will be discussed in the TEM images. The EDS analysis (shown in Fig. 3(f)) proves the existence of the elements Bi, V, O, C and N, which supports the existence of g-C_3N_4.

TEM characterization of the prepared samples was performed in order to further study the details of the morphology and microstructure of the pure g-C_3N_4, the $BiVO_4$ and the $BiVO_4$@g-C_3N_4 (Fig. 4). The g-C_3N_4 exfoliated by ultrasound had a thin nano-sheet morphology, just like the thin film with the soft edges, the wrinkled layer with some stacking layers represents the soft nanosheets (Fig. 4(a)). Fig. 4(b) shows that the pure $BiVO_4$ was ellipsoid-like with tiny bulges on its rough surface, the average size is 500 nm in diameter. The TEM images of the $BiVO_4$@g-C_3N_4 samples are shown in Fig. 4(c) and

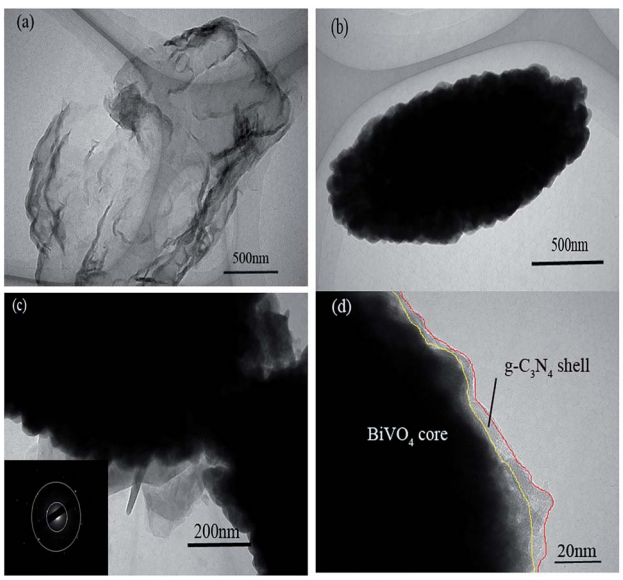

Fig. 4 TEM images of the prepared samples (a) g-C_3N_4 nano-sheets; (b) the pristine $BiVO_4$; (c) $BiVO_4$@g-C_3N_4 (the inner figure showed the SAED pattern of $BiVO_4$); (d) the structure of core–shell $BiVO_4$@g-C_3N_4.

(d). The dark black area surrounded by a gray edge represents the $BiVO_4$ core protected by the g-C_3N_4 nano-sheet shell. The thickness of g-C_3N_4 shell was about 7 nm (light-yellow lined areas). The obtained core–shell structure strengthens the tight contact between $BiVO_4$ and g-C_3N_4 nano-sheets, differs from the point contact of the loaded composites, the surface contact of core@shell structure enlarges the contact area, more contact areas does help to strengthen the synergetic effect between the π-conjugated g-C_3N_4 and inner $BiVO_4$. This not only benefits the area of light absorption, but also improves the chemical band interaction of $BiVO_4$ and g-C_3N_4, enhancing the separation efficiency of photo-induced charge, with the higher photo-degradation efficiency, this will be studied in the following discussion. The SAED pattern of $BiVO_4$ core indicates high crystallinity of $BiVO_4$ and is in agreement with the XRD analysis.

3.3. FT-IR spectra analysis

FT-IR spectra were used to characterize the special chemical bands of the prepared samples. Fig. 5 shows the FT-IR spectra of g-C_3N_4, $BiVO_4$ and $BiVO_4$@g-C_3N_4 (7 wt%). For the pure $BiVO_4$, the peak at 698 cm^{-1} represents the Bi–O bond while the 733 cm^{-1} stretching peak corresponds to $\nu_3(VO_4)$.[54] Both of them are typical peaks of $BiVO_4$.[55] The peaks at around 1400 cm^{-1} can be

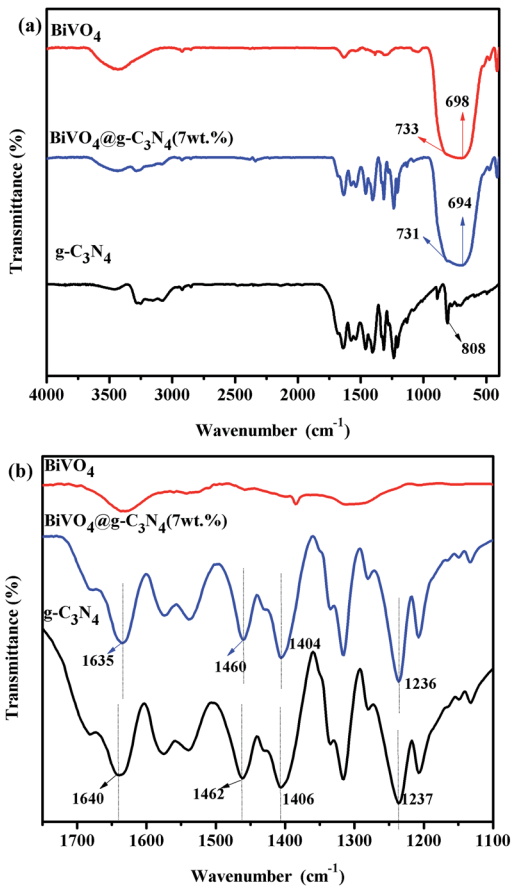

Fig. 5 (a) FTIR spectra of the prepared g-C_3N_4, $BiVO_4$ and $BiVO_4$@g-C_3N_4 photo-catalysts; (b) partial enlarged details of FTIR spectra for g-C_3N_4, $BiVO_4$ and $BiVO_4$@g-C_3N_4 between 1100–1750 cm^{-1}.

attributed to the absorption of atmospheric carbon dioxide, while the peak at 1650 cm^{-1} is characteristic of residual water on the surface.[53] The FT-IR spectra of g-C_3N_4 shows the molecular structure of the compound: there is a peak at 808 cm^{-1} that is attributed to the C–N hetero-cycle, there are bands at 1237 cm^{-1}, 1315 cm^{-1}, 1406 cm^{-1} representing the aromatic C–N stretching peaks, and a peak at 1640 cm^{-1} representing the C=N stretching. These peaks are consistent with those previously reported in literature.[25] The FT-IR spectra of core–shell $BiVO_4$@g-C_3N_4 shows both the typical stretching peaks of $BiVO_4$ and g-C_3N_4. The bands of $BiVO_4$ appear at 694 cm^{-1} and 731 cm^{-1} and are slightly red shifted when compared with pure $BiVO_4$. Likewise, the peaks of g-C_3N_4 appear at their typical positions but with a slight red shift, as seen in the enlarged portion of the FT-IR spectra in Fig. 5(b). The band strengths are weakened in the composite photocatalyst, which indicates the increased stretching of the C–N, C=N, Bi–O and V–O bonds and a more widely π-conjugated system appears between the g-C_3N_4 nano-sheets and $BiVO_4$ core.[40,56] The core–shell structure induced modified interactions between chemical bands, a covalent bond between g-C_3N_4 and $BiVO_4$ was formed, which in turn resulted in an improvement in the transfer and separation efficiency of photo-induced charges and increased photocatalytic degradation efficiency.

3.4. UV-vis analysis

UV-vis (ultraviolet-visible) absorption spectra were acquired in order to study the optical properties of the prepared samples and to further prove their photo-catalytic activity under visible light. The UV-vis of g-C_3N_4, $BiVO_4$ and $BiVO_4$@g-C_3N_4 are shown in Fig. 6(a). For pure g-C_3N_4, the edge of the absorption spectra is at about 470 nm and shows strong absorption both in the ultraviolet and partial visible regions. The UV-vis absorption spectra of the g-C_3N_4 nano-sheets shows a blue shift of about 10–20 nm in the absorption edge. As for pure $BiVO_4$, a stronger and wider absorbency is seen in visible light range. For the $BiVO_4$@g-C_3N_4 composites photo-catalyst, the absorption edge is red shifted significantly compared to g-C_3N_4, and wider light absorption is seen in the visible region. This indicates that $BiVO_4$@g-C_3N_4 may be able to absorb more light to generate electron–hole pairs. However, there was no obvious change in absorbance range between the $BiVO_4$ and the composite photo-catalysts with differing g-C_3N_4 coating amounts. $BiVO_4$@g-C_3N_4 is a direct-gap semiconductor and uses a value of $n = 2$. According to the transformed Kubelka–Munk function, the band-gap energy can be estimated by the intercept of the tangent to the plot of $(\alpha h\nu)^2$ *vs.* $(h\nu)$. The results obtained from these plots are shown in Fig. 6(b). The band-gap energy of g-C_3N_4 was found to be 2.78 eV, whereas g-C_3N_4 nano-sheet has a larger energy of 2.82 eV which might the effect of quantum confinement between the tiny nano-sheets and the larger light absorption area of the nano-sheet. The calculated band-gap energies of $BiVO_4$ and $BiVO_4$@g-C_3N_4 (3, 5, 7, 10 wt%) are both 2.45 eV, because of the little change of the edge of the absorption spectra among the samples. The effects of core@shell structure on composites photo-catalyst activity will be discussed further.

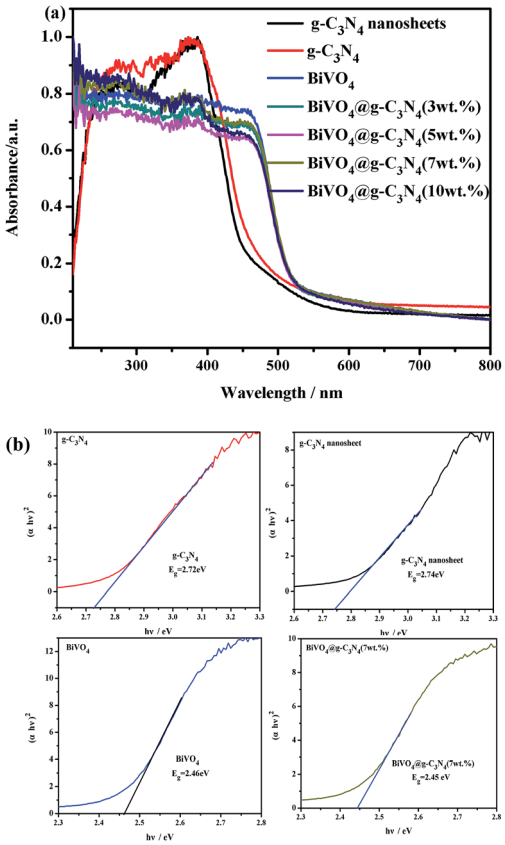

Fig. 6 (a) UV-vis diffuse reflectance spectra of prepared photo-catalysts; (b) plot of $(\alpha h\nu)^2$ *vs.* energy $(h\nu)$ and band-gap energy of the g-C_3N_4, g-C_3N_4 nano-sheet, $BiVO_4$, $BiVO_4$@g-C_3N_4 samples.

3.5. XPS spectra analysis

X-ray photoelectron spectroscopy (XPS) was performed to detect the surface chemical composition and chemical states of the prepared $BiVO_4$ and $BiVO_4$@g-C_3N_4 (7 wt%) samples. Fig. 7(a) shows the survey scan XPS spectrum of the two samples. Bi 4f, V 2p, O 1s, as well as C 1s, N 1s for the composite photo-catalyst are seen, proving that the photo-catalyst included all of the elemental components, which is in agreement with the EDS analysis results. In the core–shell $BiVO_4$@g-C_3N_4, the XPS spectra showed C 1s (Fig. 7(b)), and the binding energies of 284.8 eV and 288.05 eV are representative of the absorbed carbon on the surface and the C atom of sp^2-hybridized N–C=N bond,[57] respectively. Three peaks in the N 1s binding energy area are clearly seen (Fig. 7(c)). The peak at 397.43 eV is due to C=N–C bonds, and the other two peaks at about 398.92 eV and 401.11 eV attributed to the N atoms of N–$(C)_3$ bond and H–N–C bond,[25] respectively. For the composite photo-catalyst, the binding energies of these C 1s and N 1s peaks are typical in g-C_3N_4. In order to further study the interaction between the chemical states and core–shell structure, the XPS spectra of Bi, V and O were obtained and are depicted in Fig. 7(d)–(f). For bismuth, the typical peaks at 158.78 eV and 164.08 eV were the binding energies of Bi $4f_{7/2}$ and Bi $4f_{5/2}$, respectively, which indicates the existence of Bi^{3+} in $BiVO_4$. As for $BiVO_4$@g-C_3N_4 (7 wt%), the binding energy of Bi^{3+} was found to be slightly

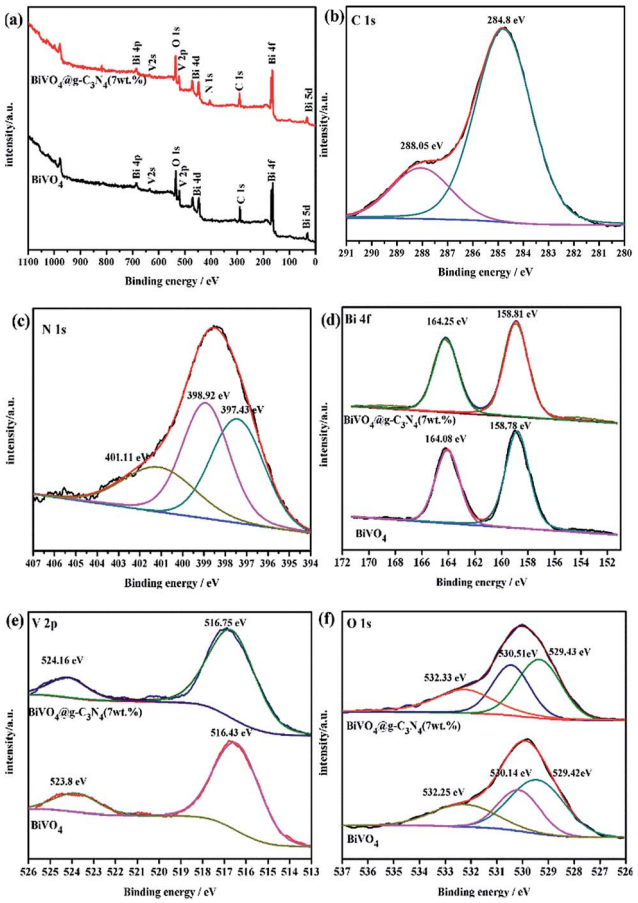

Fig. 7 (a) All XPS spectra of $BiVO_4$ and $BiVO_4$@g-C_3N_4; XPS spectra of $BiVO_4$@g-C_3N_4 (b) C 1s; (c) N 1s; XPS spectra of $BiVO_4$ and $BiVO_4$@g-C_3N_4 (d) Bi 4f; (e) V 2p; (f) O 1s.

increased (158.81 eV and 164.25 eV). For V 2p orbital, the binding energy peaks at 523.8 eV and 516.43 eV of V $2p_{1/2}$ and V $2p_{3/2}$ represent the V^{5+} in $BiVO_4$. Similarity, the peaks of V $2p_{1/2}$ and V $2p_{3/2}$ for $BiVO_4$@g-C_3N_4 (7 wt%) shift to higher binding energy at 524.16 eV and 516.75 eV (Fig. 7(e)). The XPS spectra of O 1s show three main peaks: the peak at 529.42 eV can be assigned to the lattice oxygen in $BiVO_4$, while the peaks at 530.14 eV and 532.25 eV are signals from hydroxyl groups and absorbed water on the surface of the sample. In addition, three forms of oxygen are found in the composite, the binding energies of O 1s of $BiVO_4$@g-C_3N_4 (7 wt%) are larger than those found in pure $BiVO_4$. The interaction of shell g-C_3N_4 nano-sheets and core $BiVO_4$ is confirmed by these increased binding energies,[40] the inner interaction between shell and core induces to the shift of Bi 4f, V 2p and O 1s orbitals.[58] The positive shift of binding energy means the increase of the electron density around the Bi, V, O, indicating a stronger chemical band of core–shell photo-catalyst,[45] not the simple physical mixture of $BiVO_4$ and g-C_3N_4. The π-conjugated shell g-C_3N_4 nano-sheets strengthens the chemical bonds of $BiVO_4$. The synergetic effect between the core@shell structure forms a wider π-conjugated system, the chemical interaction is strong enough to promote better separation of photo-excited electron–hole pairs, also the larger contact area does help to transfer the separated charge, effectively increasing the photo-catalysis degradation efficiency. This results support the conclusion of the FT-IR analysis.

3.6. Photocatalytic activity evaluation

Rhodamine B was employed in order to investigate the photocatalytic degradation rate of the $BiVO_4$@g-C_3N_4 samples under visible light radiation ($\lambda \geq 420$ nm). A blank experiment without any photocatalyst powder was carried out in order to quantify background degradation of RhB. The results of all experiments under irradiation for 60 min are shown in Fig. 8(a), including the blank and dark experiments as well as the RhB photo-degradation by g-C_3N_4, $BiVO_4$, and $BiVO_4$@g-C_3N_4 (x wt%). The highest degradation activity is seen when the composite contains 7% g-C_3N_4. An increase in activity is seen as the g-C_3N_4 concentration increases up to 7%, but a decrease is seen beyond this concentration at 10%. The $BiVO_4$@g-C_3N_4 (7 wt%) degraded about 90% of the RhB, a result that is 9 times greater than pure $BiVO_4$ (9%) and 1.3 times greater than pure g-C_3N_4 nano-sheets. When the g-C_3N_4 content was increased to 10%, the degradation efficiency of $BiVO_4$@g-C_3N_4 (10 wt%) decreased to 80%. The kinetic constants for the different compositions of $BiVO_4$@g-C_3N_4 were calculated (Fig. 8(b)) by assuming that the degradation rate fit the pseudo-first-order reaction model ($\ln(C_0/C_t) = kt$). When the g-C_3N_4 amounts were 1%, 3%, 5%, 7%, 10%, the values of k were 0.00435 min^{-1}, 0.00761 min^{-1}, 0.00996 min^{-1}, 0.03971 min^{-1} and 0.02661 min^{-1}, respectively. The coated amount of g-C_3N_4 nano-sheets had a great effect on the photocatalytic activity. When the g-C_3N_4 nano-sheet content was less than 7 wt%, the contact area of the core–shell structure was not large enough to promote photo-degradation. However, excessive coating with g-C_3N_4 nano-sheet might lead to resistance for the separation of electron–hole pairs and transfer. With the optimal coating amount of 7%, the larger light absorption area and π-conjugation promoted the best photocatalytic degradation efficiency, which agrees with the FT-IR and XPS results shown previously.

To further prove the effectiveness of the composite photocatalyst, a comparison of $BiVO_4$@g-C_3N_4 (7 wt%) and mechanically mixed $BiVO_4$/g-C_3N_4 (7 wt%) was performed and the results are shown in Fig. 8(c). The M-$BiVO_4$/g-C_3N_4 (7 wt%) had a similar photocatalytic performance as pure g-C_3N_4 nano-sheets, and a lower performance than $BiVO_4$@g-C_3N_4 (7 wt%). This result shows that the core–shell structure plays an important role in promoting photocatalytic activity. Fig. 8(d) shows the whole spectra scan of RhB during the photocatalytic degradation progress using $BiVO_4$@g-C_3N_4 (7 wt%), the descending peaks of RhB for other photocatalyst samples are shown in the ESI (Fig. S1†), the inner line of Fig. 8(d) is the wavelength shift of the RhB spectra under the photo irradiation of Fig. 8(d). As the symbols in red shows, the major absorption peaks of the RhB showed a blue shift from 553 nm to 497 nm gradually, the blue shift of 56 nm indicating that the RhB was mineralized by de-ethylation. De-ethylation of RhB (*N*,*N*,*N*′,*N*′-tetra-ethylated rhodamine molecule, $\lambda_{max} = 554$ nm) has the

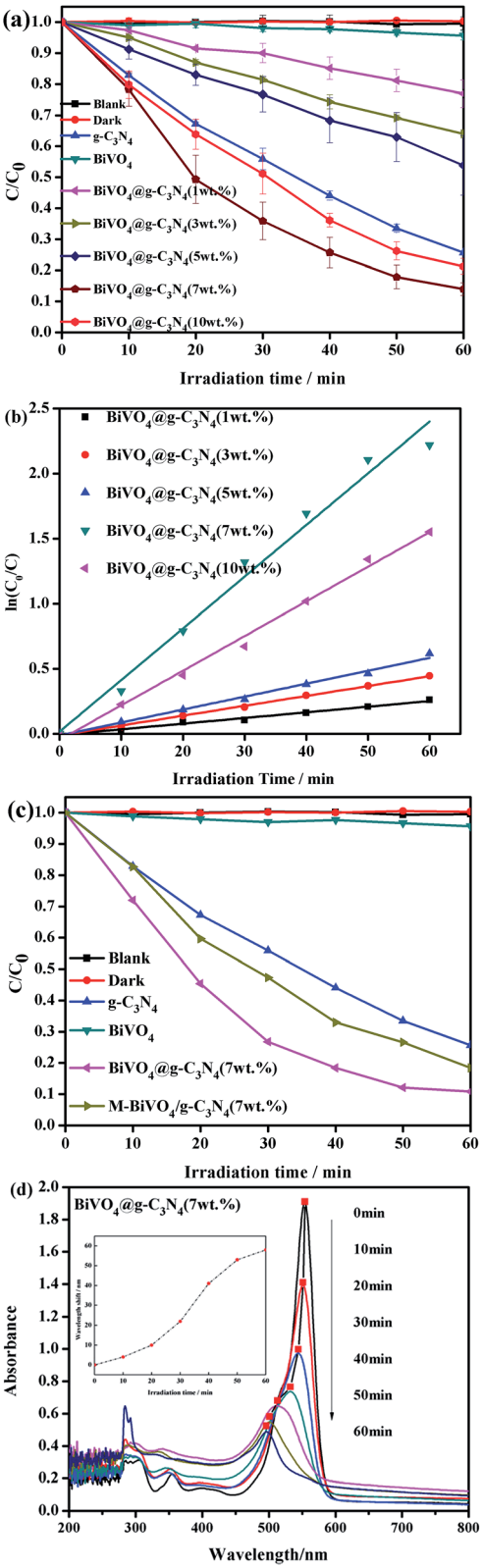

Fig. 8 (a) The comparison of photocatalytic activity for g-C_3N_4, $BiVO_4$ and $BiVO_4$@g-C_3N_4 (x wt%) (x = 1, 3, 5, 7, 10); (b) the comparison of first-order kinetic constants of different photo-catalysts; (c) the comparison of photocatalytic activity for $BiVO_4$@g-C_3N_4 (7 wt%) and M-$BiVO_4$/g-C_3N_4 (7 wt%); (d) the whole spectral scanning of RhB during the photo-catalytic degradation for $BiVO_4$@g-C_3N_4 (7 wt%).

characteristic peak shifted to the blue region, rhodamine, λ_{max} = 497 nm, the conjugated structure of stable RhB was destroyed[59,60] photocatalytically.

3.7. Trapping experiment & repeating experiment

It is well known that photo-excited electrons and holes have strong reduction and oxidation properties. This allows them to react with absorbed O_2 on the catalyst surface and generate reactive species during the photo-degradation process, such as $\cdot O_2^-$, h^+ and ·OH. In order to investigate the photocatalytic mechanism of $BiVO_4$@g-C_3N_4, a trapping experiment was designed to detect and quantify these reactive species. Benzoquinone (BQ) was added to the reaction system as a scavenger of $\cdot O_2^-$, isopropanol (IPA) was added to trap the ·OH radicals, and the ethylene diamine tetra-acetic acid disodium salt (EDTA-2Na) was used as a h^+ scavenger. The trapping experiments were maintained under the same reaction conditions as the photocatalytic activity evaluation. As seen in Fig. 9(a), the presence of IPA had little effect on the degradation rate of RhB, indicating that the ·OH radical was not the main reactive species. The degradation rate was greatly suppressed with the addition of EDTA-2Na, indicating that h^+ was an important species in the degradation of RhB. O_2^- also played an assistant role in RhB degradation. These results provide the framework for a possible photo-degradation mechanism.

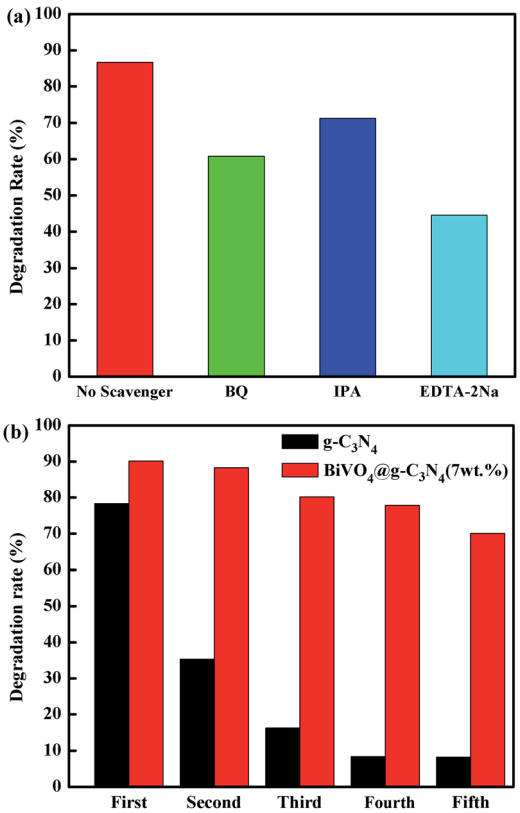

Fig. 9 (a) The comparison of degradation rate with addition of different scavengers; (b) five cycle running of photo-degradation RhB over g-C_3N_4 and $BiVO_4$@g-C_3N_4 (7 wt%).

As a high-performance photo-catalyst, it is important to evaluate the stability of prepared core–shell $BiVO_4$@g-C_3N_4 composite under visible light irradiation. In order to better study the stability and recyclability of the composite photo-catalyst, a repeating experiment of photo-degradation of RhB was carried out for five cycles. Fig. 9(b) shows the experimental degradation rate of the sample after five cycles. The pure g-C_3N_4 sample showed a great deal of instability, with the photo-degradation efficiency decreasing from 78% to 8%. Conversely, the $BiVO_4$@g-C_3N_4 (7 wt%) photocatalyst was quite stable, and the degradation rate only decreased to 75% after five recycling runs. The core–shell $BiVO_4$@g-C_3N_4 composite photo-catalyst demonstrated pretty good stability and reusability. The core–shell structure promoted chemical band interaction and stability of the composite photo-catalyst while enlarging the reaction contact area.

3.8. Photoluminescence (PL) spectra & photocurrent & EIS analysis

Photoluminescence emission spectra were obtained in order to further study the separation efficiency of electron–hole pairs. Higher intensities in the emission spectra of the sample indicate quicker recombination of photo-generated charges, thus leading to reduced photo-catalytic activity. The PL spectra of g-C_3N_4, $BiVO_4$ and $BiVO_4$@g-C_3N_4 under excitation at 320 nm are shown in Fig. 10(a). It can be clearly seen that the pure $BiVO_4$ produced strong emission peaks around 520 nm.[61] The relative intensity of $BiVO_4$ was much greater than that of $BiVO_4$@g-C_3N_4, and the PL intensity of g-C_3N_4 was also greater, indicating that coating with g-C_3N_4 nano-sheets played an important role in suppressing the recombination of electrons and holes. The core–shell structure resulted in an improvement in the separation efficiency of photo-generated charges. Fig. 10(b) shows a magnified view of the PL spectra of $BiVO_4$@g-C_3N_4 (x wt%) (x = 3, 5, 7, 10). With increasing g-C_3N_4 content, the intensities of PL decrease until the content reaches 7%, after which the intensity increases. This may be due to an excess in g-C_3N_4 nano-sheets on the surface resulting in a gradual disappearance of the π-conjugated synergetic effect. These results are in agreement with the photo-catalytic activity results.

In order to provide more evidence of photoelectron and hole separation, a transient photocurrent response experiment was performed under visible light irradiation every 30 seconds. A higher photocurrent response value indicates lower recombination and more efficient separation of electron–hole pairs.[62] As the results in Fig. 11 show, the semiconductor electrodes modified by the $BiVO_4$, g-C_3N_4 and $BiVO_4$@g-C_3N_4 samples show quick photocurrent response under the light irradiation, and decrease to zero immediately as soon as the light off. The $BiVO_4$@g-C_3N_4 composite conducts the most photocurrent when compared with both pure $BiVO_4$ and g-C_3N_4. Namely, more electron–hole pairs can be separated efficiently over the $BiVO_4$@g-C_3N_4 sample, and the longer lifetime of the photo-excited charge carrier than that of pure $BiVO_4$, g-C_3N_4. In this case, the core–shell structure resulted in a larger contact area which contributed to a higher photocurrent response and

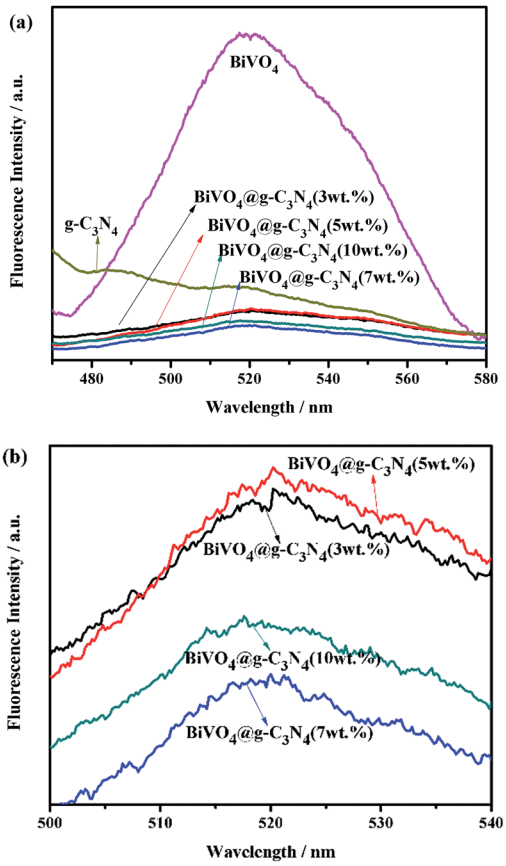

Fig. 10 (a) Photoluminescence spectra of as-prepared g-C_3N_4, $BiVO_4$, $BiVO_4$@g-C_3N_4; (b) partial enlarged PL spectra of $BiVO_4$@g-C_3N_4 with different amounts of g-C_3N_4 nano-sheets.

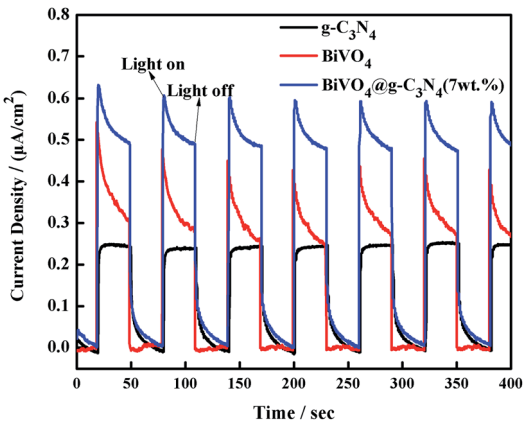

Fig. 11 Transient photocurrent response for g-C_3N_4, $BiVO_4$ and $BiVO_4$@g-C_3N_4 photo-catalysts.

inhibited the recombination rate of photo-excited reactive electrons and holes.

Electrochemical impedance spectroscopy (EIS) of pure g-C_3N_4, $BiVO_4$ and $BiVO_4$@g-C_3N_4 was performed in order to investigate the charge transfer resistance and assess the separation efficiency of electron–hole pairs, which is a crucial factor for photocatalytic degradation. In the Nyquist diagram of EIS,

a smaller radius is evidence of smaller charge transfer resistance and a faster charge transfer rate.[63] Fig. 12 shows that the arc radius of $BiVO_4$@g-C_3N_4 (7 wt%) is the smallest among the three samples. The core–shell structure formed between $BiVO_4$ and the g-C_3N_4 nano-sheets changed the chemical bands and altered the resistance on the electrode surface, resulting in higher separation efficiency and a faster transfer rate of photo-generated charges. As the widely conjugated system developed, just as the FT-IR and XPS analysis, the interaction between g-C_3N_4 nano-sheets shell and $BiVO_4$ core can provide an effective path for the transfer of photo-induced charges. These datas also support the results from the photocatalytic activity, PL, and photocurrent results.

3.9. The proposed mechanism of photocatalytic degradation

Based on the analysis and characterization of the experimental results above, a possible photocatalytic mechanism for core–shell $BiVO_4$@g-C_3N_4 is proposed and discussed below. The layered g-C_3N_4 nano-sheets coated on the ellipsoid-like $BiVO_4$ provide a larger contact area and interface between the core and shell, resulting in strengthening of the π-conjugated system and promotion of the separation of photo-generated electron–hole pairs. This enables a higher photo-degradation efficiency under light irradiation. Proper band gap position of the photo-catalyst is one of the key factors to promote separation of electron–hole pairs and is a result of the composite's properties. According to the data from the UV-vis experiments, the band-gap energy of $BiVO_4$ is 2.46 eV (Fig. 5(b)). The band gap edge positions of the conduction band and valence band can be calculated by the formulas:

$$E_{CB} = X - E^e - 0.5E_g,\ E_{VB} = E_{CB} + E_g$$

where X represents the absolute electronegativity of the semi-conductor and is obtained from the geometric mean of the constituent atoms, E^e is the energy of free electrons on the hydrogen scale (about 4.5 eV), and E_g is the band-gap energy of the semiconductor.[64] The E_{CB} and E_{VB} values were 0.31 eV and 2.77 eV for $BiVO_4$, respectively. For g-C_3N_4, the conduction band and valence band were found at −1.13 eV and 1.57 eV, which agrees with previously reported literature values.[45] A proposed mechanism that considers the relative band gap edge positions is illustrated in Fig. 13. Under the irradiation of visible light, both $BiVO_4$ and g-C_3N_4 are excited and easily induce the generation of electron–hole pairs. Due to the well-matched band structure and large interfacial contact area of the core–shell structure, the photo-excited electrons of g-C_3N_4 are easily transferred to the CB of $BiVO_4$. Simultaneously, the holes in the VB of $BiVO_4$ easily migrate to the VB of g-C_3N_4 shell, where they are able to oxidize the absorbed RhB molecules into micro molecules. As the CB edge potential of g-C_3N_4 is more negative than the reduction potential of $O_2/\cdot O_2^-$ (−0.33 eV),[65] during the excited electrons migrated from conduction band of g-C_3N_4 to $BiVO_4$, only part of the electrons are able to reduce the absorbed oxygen into superoxide radicals ($\cdot O_2^-$), some of the electrons transported to the CB of $BiVO_4$. As was described in the trapping experiment, the h^+ are the main reactive species and the $\cdot O_2^-$ are an assistant species. The core–shell structure of the composite photo-catalyst facilitates efficient separation of photo-induced electron–hole pairs, and the layered shell provides more active sites due to an enlarged contact area. The wider π-conjugated system of the core–shell structure, the thin shell material reduces the distance for migration, allowing for more photo-excited charges to be separated and transferred.

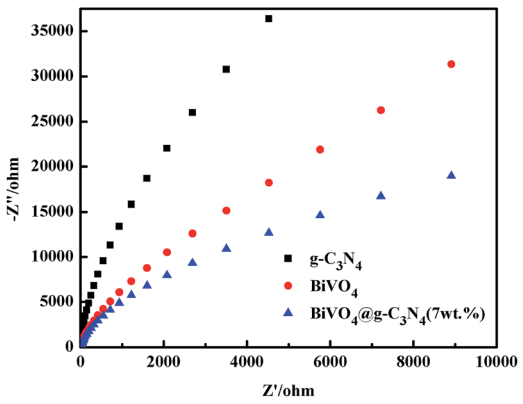

Fig. 12 Electrochemical impedance spectroscopy of g-C_3N_4, $BiVO_4$ and $BiVO_4$@g-C_3N_4.

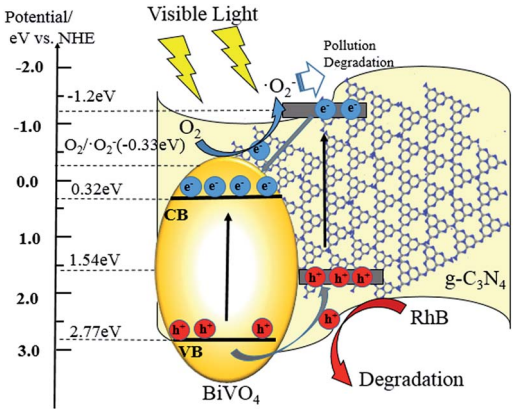

Fig. 13 The proposed mechanism for photo-degradation process.

4. Conclusions

Ellipsoid-like $BiVO_4$ and core–shell structured $BiVO_4$@g-C_3N_4 were successfully synthesized through a hydrothermal and ultra-sonicated-chemisorption method. Ellipsoid-like $BiVO_4$ was prepared through the addition of ethylene glycol. The performance of the composite photo-catalyst was accessed by evaluating its ability to degrade RhB pollution in water. The highest photo-degradation efficiency occurred when the content of g-C_3N_4 nano-sheet was 7% and was 9 times greater than that of pure $BiVO_4$. In addition, the core–shell $BiVO_4$@g-C_3N_4 showed high stability after five cycles of light irradiation. The stable core–shell structure of the composite photo-catalyst not only enlarged the contact area, but also strengthened the interaction of chemical bands, effectively enhancing the π-

conjugation. This resulted in efficient separation of the photo-excited electron–hole pairs and a high rate of photo-degradation of RhB (90% degradation in 60 min). This promising novel core–shell composite photo-catalyst provides an exciting area for further application and study.

Acknowledgements

This work was funded by the National Natural Science Foundation of China (grant No. 21476161), Key Program of Natural Science of Hebei Province (B2016209375), Hebei Provincial Foundation for International Cooperation (No. 15391403D) and National Science and Engineering Research Council of Canada (Discovery).

Notes and references

1 A. Fujishima and K. Honda, *Nature*, 1972, **238**, 37–38.
2 H. Tong, S. Ouyang, Y. Bi, N. Umezawa, M. Oshikiri and J. Ye, *Adv. Mater.*, 2012, **24**, 229–251.
3 C. McCullagh, N. Skillen, M. Adams and P. K. J. Robertson, *J. Chem. Technol. Biotechnol.*, 2011, **86**, 1002–1017.
4 D. Chatterjee and S. Dasgupta, *J. Photochem. Photobiol., C*, 2005, **6**, 186–205.
5 X. Chen, Y. Dai and X. Wang, *J. Alloys Compd.*, 2015, **649**, 910–932.
6 M. Pelaez, N. T. Nolan, S. C. Pillai, M. K. Seery, P. Falaras, A. G. Kontos, P. S. M. Dunlop, J. W. J. Hamilton, J. A. Byrne, K. O'Shea, M. H. Entezari and D. D. Dionysiou, *Appl. Catal., B*, 2012, **125**, 331–349.
7 M. Ni, M. K. H. Leung, D. Y. C. Leung and K. Sumathy, *Renewable Sustainable Energy Rev.*, 2007, **11**, 401–425.
8 Z. Yi, J. Ye, N. Kikugawa, T. Kako, S. Ouyang, H. Stuart-Williams, H. Yang, J. Cao, W. Luo, Z. Li, Y. Liu and R. L. Withers, *Nat. Mater.*, 2010, **9**, 559–564.
9 X. Zhang, X. B. Wang, L. W. Wang, W. K. Wang, L. L. Long, W. W. Li and H. Q. Yu, *ACS Appl. Mater. Interfaces*, 2014, **6**, 7766–7772.
10 J. Xia, S. Yin, H. Li, H. Xu, Y. Yan and Q. Zhang, *Langmuir*, 2011, **27**, 1200–1206.
11 J. Zhang, F. Shi, J. Lin, D. Chen, J. Gao, Z. Huang, X. Ding and C. Tang, *Chem. Mater.*, 2008, **20**, 2937–2941.
12 H. Huang, X. Han, X. Li, S. Wang, P. K. Chu and Y. Zhang, *ACS Appl. Mater. Interfaces*, 2015, **7**, 482–492.
13 H. Huang, K. Xiao, Y. He, T. Zhang, F. Dong, X. Du and Y. Zhang, *Appl. Catal., B*, 2016, **199**, 75–86.
14 S. Guo, X. Li, H. Wang, F. Dong and Z. Wu, *J. Colloid Interface Sci.*, 2012, **369**, 373–380.
15 D. Sánchez-Martínez, D. B. Hernández-Uresti, L. M. Torres-Martinez and S. Mejia-Rosales, *Res. Chem. Intermed.*, 2015, **41**, 8839–8854.
16 B.-X. Lei, L.-L. Zeng, P. Zhang, Z.-F. Sun, W. Sun and X.-X. Zhang, *Adv. Powder Technol.*, 2014, **25**, 946–951.
17 T. Saison, N. Chemin, C. Chanéac, O. Durupthy, L. Mariey, F. Maugé, V. Brezová and J.-P. Jolivet, *J. Phys. Chem. C*, 2015, **119**, 12967–12977.
18 O. F. Lopes, K. T. G. Carvalho, A. E. Nogueira, W. Avansi and C. Ribeiro, *Appl. Catal., B*, 2016, **188**, 87–97.
19 S. Obregón, A. Caballero and G. Colón, *Appl. Catal., B*, 2012, **117–118**, 59–66.
20 W. Wang, X. Huang, S. Wu, Y. Zhou, L. Wang, H. Shi, Y. Liang and B. Zou, *Appl. Catal., B*, 2013, **134–135**, 293–301.
21 C. Li, P. Zhang, R. Lv, J. Lu, T. Wang, S. Wang, H. Wang and J. Gong, *Small*, 2013, **9**, 3951–3956.
22 S. Dong, Y. Cui, Y. Wang, Y. Li, L. Hu, J. Sun and J. Sun, *Chem. Eng. J.*, 2014, **249**, 102–110.
23 M. L. Guan, D. K. Ma, S. W. Hu, Y. J. Chen and S. M. Huang, *Inorg. Chem.*, 2011, **50**, 800–805.
24 W. Zhao, Y. Liu, Z. Wei, S. Yang, H. He and C. Sun, *Appl. Catal., B*, 2016, **185**, 242–252.
25 X.-S. Zhang, J.-Y. Hu and H. Jiang, *Chem. Eng. J.*, 2014, **256**, 230–237.
26 T. Zhu, Y. Song, H. Ji, Y. Xu, Y. Song, J. Xia, S. Yin, Y. Li, H. Xu, Q. Zhang and H. Li, *Chem. Eng. J.*, 2015, **271**, 96–105.
27 X. Wang, K. Maeda, A. Thomas, K. Takanabe, G. Xin, J. M. Carlsson, K. Domen and M. Antonietti, *Nat. Mater.*, 2009, **8**, 76–80.
28 H. Yan and H. Yang, *J. Alloys Compd.*, 2011, **509**, L26–L29.
29 K. Sridharan, E. Jang and T. J. Park, *Appl. Catal., B*, 2013, **142–143**, 718–728.
30 L. Ge, F. Zuo, J. Liu, Q. Ma, C. Wang, D. Sun, L. Bartels and P. Feng, *J. Phys. Chem. C*, 2012, **116**, 13708–13714.
31 X. Dai, M. Xie, S. Meng, X. Fu and S. Chen, *Appl. Catal., B*, 2014, **158–159**, 382–390.
32 H. Xu, J. Yan, Y. Xu, Y. Song, H. Li, J. Xia, C. Huang and H. Wan, *Appl. Catal., B*, 2013, **129**, 182–193.
33 H. Shi, C. Zhang and C. Zhou, *RSC Adv.*, 2015, **5**, 50146–50154.
34 N. Tian, H. Huang, C. Liu, F. Dong, T. Zhang, X. Du, S. Yua and Y. Zhang, *J. Mater. Chem. A*, 2015, **3**, 17120–17129.
35 L. Ge, C. Han and J. Liu, *Appl. Catal., B*, 2011, **108–109**, 100–107.
36 L. Liu, Y. Qi, J. Lu, S. Lin, W. An, J. Hu, Y. Liang and W. Cui, *RSC Adv.*, 2015, **9**, 99339–99346.
37 C. Liu, H. Huang, X. Du, T. Zhang, N. Tian, Y. Guo and Y. Zhang, *J. Phys. Chem. C*, 2015, **119**, 17156–17165.
38 P. Niu, L. Zhang, G. Liu and H.-M. Cheng, *Adv. Funct. Mater.*, 2012, **22**, 4763–4770.
39 L. Liu, Y. Qi, J. Lu, S. Lin, W. An, Y. Liang and W. Cui, *Appl. Catal., B*, 2016, **183**, 133–141.
40 S. Kumar, A. Baruah, S. Tonda, B. Kumar, V. Shanker and B. Sreedhar, *Nanoscale*, 2014, **6**, 4830–4842.
41 N. Tian, H. Huang, Y. He, Y. Guo, T. Zhang and Y. Zhang, *Dalton Trans.*, 2015, **44**, 4297–4307.
42 H. J. Kong, D. H. Won, J. Kim and S. I. Woo, *Chem. Mater.*, 2016, **28**, 1318–1324.
43 Y. Ji, J. Cao, L. Jiang, Y. Zhang and Z. Yi, *J. Alloys Compd.*, 2014, **590**, 9–14.
44 C. Li, S. Wang, T. Wang, Y. Wei, P. Zhang and J. Gong, *Small*, 2014, **10**, 2783–2790.
45 M. Ou, Q. Zhong and S. Zhang, *J. Sol-Gel Sci. Technol.*, 2014, **72**, 443–454.

46 Z. Li, M. Li, Z. Bian, Y. Kathiraser and S. Kawi, *Appl. Catal., B*, 2016, **188**, 324–341.
47 S. W. Hu, L. W. Yang, Y. Tian, X. L. Wei, J. W. Ding, J. X. Zhong and P. K. Chu, *Appl. Catal., B*, 2015, **163**, 611–622.
48 M. Ge, L. Liu, W. Chen and Z. Zhou, *CrystEngComm*, 2012, **14**, 1038–1044.
49 L. Ge, C. Han, J. Liu and Y. Li, *Appl. Catal., A*, 2011, **409–410**, 215–222.
50 G. Liao, S. Chen, X. Quan, H. Yu and H. Zhao, *J. Mater. Chem.*, 2012, **22**, 2721–2726.
51 X. Zhang, X. Xie, H. Wang, J. Zhang, B. Pan and Y. Xie, *J. Am. Chem. Soc.*, 2013, **135**, 18–21.
52 H. Li, K. Yu, X. Lei, B. Guo, H. Fu and Z. Zhu, *J. Phys. Chem. C*, 2015, **119**, 22681–22689.
53 J. Liu, H. Wang, S. Wang and H. Yan, *Mater. Sci. Eng., B*, 2003, **104**, 36–39.
54 M. Yang and X. Jin, *J. Wuhan Univ. Technol., Mater. Sci. Ed.*, 2015, **30**, 217–222.
55 M. Gotić, S. Musić, M. Ivanda, M. Šoufek and S. Popović, *J. Mol. Struct.*, 2005, **744–747**, 535–540.
56 Y. Wang, R. Shi, J. Lin and Y. Zhu, *Energy Environ. Sci.*, 2011, **4**, 2922.
57 S. C. Yan, Z. S. Li and Z. G. Zou, *Langmuir*, 2010, **26**, 3894–3901.
58 S. Wang, D. Li, C. Sun, S. Yang, Y. Guan and H. He, *Appl. Catal., B*, 2014, **144**, 885–892.
59 T. Wu, G. Liu and J. Zhao, *J. Phys. Chem. B*, 1998, **102**, 5845–5851.
60 M. Yan, Y. Wu, Y. Yan, X. Yan, F. Zhu, Y. Hua and W. Shi, *ACS Sustainable Chem. Eng.*, 2016, **4**, 757–766.
61 D. K. Ma, M. L. Guan, S. S. Liu, Y. Q. Zhang, C. W. Zhang, Y. X. He and S. M. Huang, *Dalton Trans.*, 2012, **41**, 5581–5586.
62 Y. Xu, H. Xu, L. Wang, J. Yan, H. Li, Y. Song, L. Huang and G. Cai, *Dalton Trans.*, 2013, **42**, 7604–7613.
63 J. Kim, S. Byun, A. J. Smith, J. Yu and J. Huang, *J. Phys. Chem. Lett.*, 2013, **4**, 1227–1232.
64 J. Zhang, F. Ren, M. Deng and Y. Wang, *Phys. Chem. Chem. Phys.*, 2015, **17**, 10218–10226.
65 J. Kim, C. W. Lee and W. Choi, *Environ. Sci. Technol.*, 2010, **44**, 6849–6854.